Received: 12 April 2024 | Revised: 26 August 2024 | Accepted: 25 October 2024

DOI: 10.1002/aic.18641

AIChE JOURNAL

RESEARCH ARTICLE

Particle Technology and Fluidization

Combing mobile electrical capacitance tomography with Fourier neural operator for 3D fluidized beds measurement

Cheng Zhang[1,2] | Anqi Li[3] | Chenggong Li[1] | Xue Li[1] | Mao Ye[1] | Zhongmin Liu[1]

[1]Dalian Institute of Chemical Physics, Chinese Academy of Sciences, Dalian, People's Republic of China

[2]University of Chinese Academy of Sciences, Beijing, People's Republic of China

[3]School of Chemistry and Chemical Engineering, Chongqing University, Chongqing, People's Republic of China

Correspondence
Xue Li and Mao Ye, Dalian Institute of Chemical Physics, Chinese Academy of Sciences, Dalian, 116023, People's Republic of China.
Email: lixue@dicp.ac.cn and maoye@dicp.ac.cn

Funding information
The National Natural Science Foundation of China, Grant/Award Numbers: 22108269, 22293021, 22288101; DICP Innovation Foundation, Grant/Award Number: I202238

Abstract

Despite the practical importance, 3D measurements of gas–solid distribution in fluidized beds calls for further breakthroughs. Here an approach combing a recently developed mobile electrical capacitance tomography (ECT) sensor with Fourier Neural Operator (FNO) is developed, in which the fluidized bed is divided into a series of cross-sectional slices along axial direction. At any given instant, the gas–solid distribution in one slice is measured by mobile ECT and the others, meantime, are predicted by FNO pre-trained using experimental data. We verified this approach via computational fluid dynamics (CFD) simulations and experimental measurement of static object (i.e., cone, cylinder, and sphere) in fluidized bed. Following we applied this approach to direct measure 3D gas–solid distribution in a bubbling fluidized bed, and found that satisfactory image correlation coefficients and solid concentration average absolute deviation could be obtained, which indicates the proposed approach is promising for 3D fluidized bed measurements.

KEYWORDS
3D measurement, deep fluidized bed, Fourier neural operator, mobile electrical capacitance tomography

1 | INTRODUCTION

Gas–solid two-phase flow in fluidized beds, normally showing multi-scale, dynamic, and nonlinear characteristics,[1–4] poses important effects on heat and mass transfer as well as chemical reaction in industrial processes. Obtaining detailed gas–solid two-phase distribution and understanding the underlying hydrodynamics are of practical significance in designing and optimizing industrial processes using fluidized bed reactors.[5–7] Lots of theoretical analysis and numerical simulations have been conducted in the past decades to study the hydrodynamics in fluidized beds. However, the verification and validation of theoretical analysis[8,9] and numerical simulations[10–12] rely essentially on reliable measurement data. Moreover, the development of measurement techniques capable of capturing three-dimensional gas–solid distributions inside fluidized beds still remains a highly desired yet challenging task owing to the non-transparency nature of the reactor vessels.

Basically gas–solid fluidized bed measurement methods can be divided into three categories: intrusive methods,[13–16] non-invasive methods,[17–19] and tracer methods.[20–22] Among them, the non-invasive measurement methods are featured as no interference with fluid flows inside the reactors. Electrical capacitance tomography (ECT) is one of the non-invasive measurement technologies that has been receiving increasing attention due to the high temporal resolution, lack of radiation, and low cost.[23–27] The principle of ECT lies in that gas and solids have different permittivity, and the change of gas–solid distribution alters the equivalent permittivity (and thus the capacitance) between each pair of electrodes in the ECT sensor. By use of image reconstruction algorithms,[28–30] the measured capacitance distribution can be inverted into the permittivity distribution of the bed,

which will then be mapped to gas–solid distribution (or solids concentration distribution).[31] Traditionally the electrodes of ECT sensor installed on the external surface of the wall of fluidized beds have rectangular shape with regular arrangement, which are primarily used to measure the 2D cross-sectional gas–solid distributions.[32] 3D ECT represents a promising direction for fluidized bed measurements as it can offer volumetric images, and directly visualize the complex flow patterns as well as gas bubbles inside fluidized beds.[27,33,34] Basically, there are two ways to realize the 3D ECT in fluidized bed measurements. One way is to use the time series of single-layer 2D cross-sectional images to reconstruct 3D images,[35–37] which, however, is limited to the steady flow patterns and might suffer from the distortion of 3D images due to the average effect along the axial direction.[24,38] Another way is to use the specially designed multi-plane electrodes to obtain the volumetric images,[39–41] for example, the three or four planes of rectangular electrodes arranged inline[42] or staggered irregular electrodes.[43] In this way, the signal-to-noise ratio needs to be enhanced as the measured signals between electrodes far from each other will be very weak.[44–46] Therefore, 3D ECT measurement of fluidized beds is still in its infancy and calls for further breakthroughs in either sensor or reconstruction algorithms.

In recent work, we have developed a mobile ECT sensor that had been successfully used to measure the 2D cross-sectional gas–solid distributions at different axial positions in a deep fluidized bed. Though it is possible to apply the mobile ECT to obtain the gas–solid distribution along the axial direction, the constraint is that the measurements at different axial positions cannot be conducted simultaneously.

It has been shown that the data-driven machine learning (ML) methods can be effectively used to either reconstruct the missing flow field or predict the future flow field based on the measured data.[47–50] For instance, Ma et al. adopted the skip-connection convolutional neural network (CNN), based on dimension reduction and feature capturing, to successfully reconstruct and predict the high dimensional and nonlinear flows around a single particle with small noised datasets obtained by particle image velocimetry (PIV) experiments.[47] Fukami et al. used CNN to reconstruct the high-resolution flow field from grossly under-resolved turbulent flow field data.[48] Eavizi et al. applied the long short-term memory (LSTM) neural network to predict the velocity field of unsteady flows at future time instants.[49] Nakamura also employed LSTM to derive the temporal evolution of a turbulent channel flow.[50]

Recently Li et al. proposed a Fourier neural operator (FNO) to solve parametric partial differential equations and found that FNO manifests superior performance in solving governing equations of fluid flows with improved speed and zero-shot super-resolution.[51] In this regard, FNO might offer a faster and more accurate approach for fluid flow reconstruction and prediction than traditional machine learning methods.

In this work, therefore, we intend to combine mobile ECT with FNO based machine learning method to obtain instantaneous 3D gas–solid distribution in fluidized beds. This paper is organized as follows: We first introduce the working scheme of mobile ECT and FNO method, as well as the strategy of 3D gas–solid distribution measurement by combining mobile ECT and FNO. Next, we verify our proposed approach by reconstructing multi-layer gas–solid distribution in fluidized beds based on numerical simulations. Then, we show the feasibility of our approach through ECT measurements of static objects in an empty fluidized bed. Finally, we demonstrate the effectiveness of our approach with ECT experiments of a deep fluidized bed, focusing on the 3D gas–solid distribution and key hydrodynamic parameters such as average solid concentration and equivalent bubble diameter.

2 | METHODOLOGY

2.1 | ECT sensors and fluidized beds

Two sensors were used in the experiments: one was a single-plane eight-electrode ECT sensor, and the other was a mobile dual-plane 16-electrode ECT sensor. The former was used for measuring the static objects and the latter was used for gas–solid distribution measurement in fluidized beds. Each electrode in the eight-electrode ECT sensor was 20 mm long and 20 mm wide, with two shaft end shield electrodes which were respectively 8 mm far from the measuring electrodes, protecting signals from external electromagnetic interference. All the electrodes were directly attached to a glass tube with wall thickness of 2.5 mm and inner diameter of 61 mm.

The mobile dual-plane 16-electrode ECT sensor was composed of two measuring electrode sliders and three shielding sliders including two shaft end shield electrodes and one inter-electrode shield electrode, as shown in Figure 1. Shielding sliders were used to eliminate static interference and reduce the connection of electrical signals between electrode planes. The effective length of electrode sheet was 30 mm with 0.1 mm thickness, and the ratio of electrode to gap was 4:1. The main design parameters of the sensor were referred to the work by Huang et al.[38] The main difference between the mobile ECT sensor and fixed ECT sensor was that the electrode sheet was attached to the inner wall of the slider instead of fluidized bed tube wall. The constraint of both, however, was that the measurements at different axial positions could not be conducted simultaneously.

A quartz fluidized bed reactor was used in this study, which was 1000 mm long and had an inner diameter of 60 mm, and wall thickness of 2.5 mm. Compressed air flowed into the bed from the bottom through a gas-distributor with the superficial gas velocity of 20.6 mm/s. The particles used in the experiments were Al_2O_3 powder with a particle density of 3900 kg/m^3, a sauter mean diameter of 79.16 μm. The minimum fluidization velocity for this powder was 14.5 mm/s. The solid fraction of the packed bed at the beginning of experiments was 0.43 with a static bed height of 600 mm. In all experiments, a 16-channel AC ECT signal processing system (ECT Instruments Ltd., UK) was used, and the capacitance was measured via a double-plane single-electrode excitation mode with the mobile ECT sensor under the excitation frequency of 180 kHz and the excitation voltage of 20 Vp-p.[52] It should be note that a sufficiently round quartz tube was made as fluidized bed in this work. This ensures the slider of mobile ECT passing the tube evenly and thereby reducing the effect of non-uniform air gap between ECT electrodes and the outside wall of the

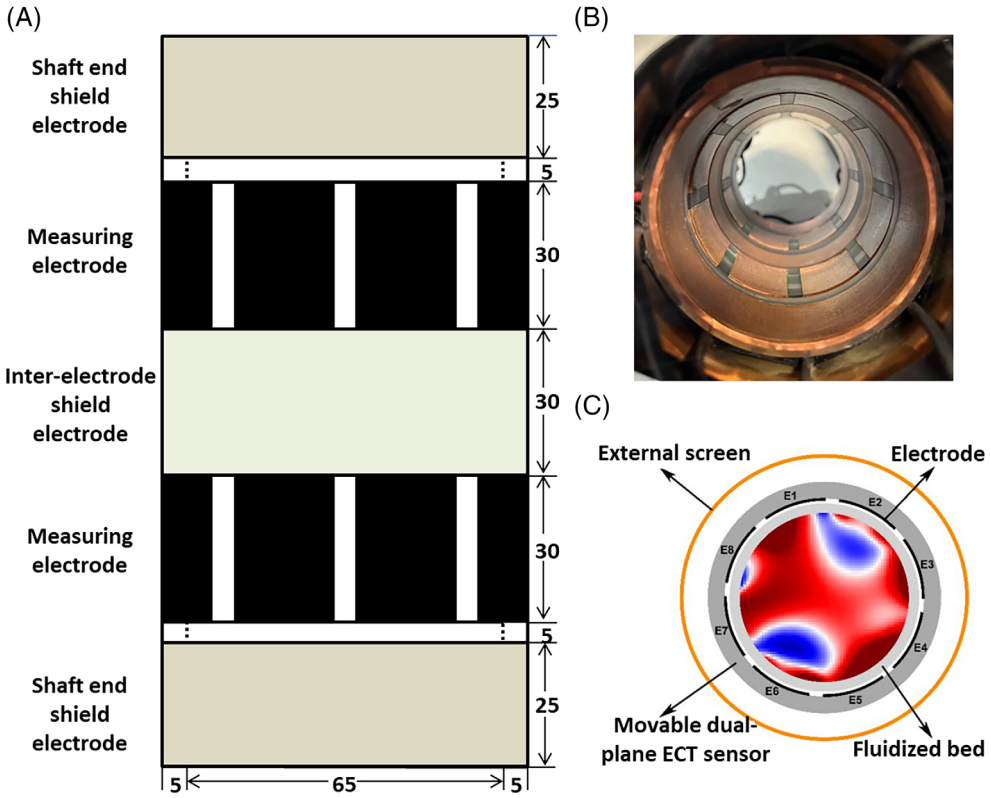

FIGURE 1 Mobile ECT sensor: (A) electrode arrangement, (B) actual top view of the sensor, and (C) cross-sectional schematic diagram.

tube on capacitance measurement. In order to obtain gas–solid distribution along axial direction, nine different cross-sectional slices, which were respectively located at the height of 6, 12, 18, 24, 30, 36, 42, 48, and 54 cm (marked as 0.1, 0.2, 0.3, 0.4, 0.5, 0.6, 0.7, 0.8, and 0.9 h correspondingly in the rest of this paper) from the bottom of the reactor, were considered. For the measurement of gas–solid at each slice, we will repeat the experiments five times using the mobile ECT sensor. In each measurement, the data sampling was carried out when the fluidized bed reached a stable fluidization after 5 min. A total of 5000 frames with 200 frames per second were recorded for each measurement with mobile ECT. One frame is recorded for each movement based our proposed method, so it takes 0.005 s to move to another slice. The distance between adjacent slices is 6 cm. Therefore, the moving speed of the mobile ECT is 12 m/s. As for numerical simulation, the sampling frequency is 100 frames per second. The distance between hypothetic adjacent slices is 5 cm for bubbling fluidization and 4 cm for turbulent fluidization. So the moving speed is 5 and 4 m/s, respectively.

During the measurement, the electric field inside the ECT sensor can be described as Equation (1),

$$\nabla[\varepsilon_r(x,y)\nabla\varphi(x,y)] = 0 \tag{1}$$

where $\varepsilon_r(x,y)$ is the mixed permittivity distribution and $\varphi(x,y)$ is the potential distribution. Then we can obtain the mixed capacitance C_M:

$$C_M = -\varepsilon_0 \frac{1}{V}\int\int \varepsilon_r(x,y)\nabla\varphi(x,y)d\Gamma \tag{2}$$

with ε_0 representing the permittivity of the vacuum environment.[29]

Equation (2) can be rewritten as

$$\lambda = SG \tag{3}$$

where λ is the normalized capacitance defined as

$$\lambda = \frac{C_M - C_L}{C_H - C_L} \tag{4}$$

and G is the normalized permittivity defined as

$$G = \frac{\varepsilon_r(x,y) - \varepsilon_L}{\varepsilon_H - \varepsilon_L} \tag{5}$$

From Equation (4), it is shown that C_H and C_L are the high capacitance and low capacitance during normalization, and ε_H and ε_L are the relative permittivity of solid particles and gas phases, respectively. S is the normalized matrix of sensitive field,

$$S = \frac{s_{ij}^*}{\sum_{n=1}^{N} s_{ij}^*} \tag{6}$$

with

$$S_{ij}^*(x,y) = -\int\int \frac{\nabla\varphi_i(x,y)}{V_i}\frac{\nabla\varphi_j(x,y)}{V_j}dxdy \tag{7}$$

where V is the voltage. Note that the subscripts i and j present the potential distribution $\nabla\varphi_i(x,y)$ and $\nabla\varphi_j(x,y)$ captured by the i^{th} and the j^{th} electrode, respectively.

Thus the permittivity distribution can be obtained from the measured capacitance by solving the inverse problem of Equation (3):

$$G = S^{-1}\lambda \tag{8}$$

It should be noted that there are many reconstruction algorithms developed to solve the ill-posed problem as shown by Equation (8).[30] Here we used the Landweber iteration algorithm, the most commonly used benchmark algorithm, due to the robustness and excellence in ECT image reconstruction. Equations (9)–(12) show the scheme of Landweber iteration algorithm[53]:

$$\widehat{G}_k = P\left(\widehat{G}_{k-1} + \alpha_k s^T e_{k-1}\right) \tag{9}$$

$$p[f(x)] = \begin{cases} 0 f(x) < 0 \\ f(x)\, 0 \le f(x) \le 1 \\ 1 f(x) > 1 \end{cases} \tag{10}$$

$$\alpha_k = \frac{\left\| s^T e_{k-1} \right\|}{\left\| S S^T e_{k-1} \right\|} \tag{11}$$

$$e_{k-1} = \lambda - S\widehat{G}_{k-1} \tag{12}$$

where k is index of iteration number, α is a parameter (in the range of 1–2) controlling iteration step, and e_{k-1} is the difference between actual capacitance and capacitance calculated by the forward problem of the $k-1$th iteration. In this work, we judged the convergence end point by pre-setting the number of iteration.

After obtaining the permittivity distribution by Equation (8), we could then acquire the concentration distribution via concentration model.[30,54,55] The parallel model is the most widely used concentration model, as shown in the following:

$$\widehat{\beta} = \widehat{G} \tag{13}$$

$$\widehat{\phi} = \theta\widehat{\beta} \tag{14}$$

where $\widehat{\beta}$ is the normalized solid phase volume fraction, θ is the solid phase volume fraction in the fixed bed state, and $\widehat{\phi}$ is solid phase concentration distribution in the measurement section which can be obtained according to Equation (14).

Following the principle described above, we can obtain the gas solid concentration distribution based on the permittivity distribution by parallel model, with the permittivity distribution being reconstructed from the measured capacitance by Landweber iteration algorithm.

2.2 | Fourier neural operator

Machine learning (ML) methods can be effectively used to predict the future flow field based on the measured data.[49] FNO is a grid-free solution operator that is improved over traditional CNN.[51] We had verified that prediction ability of FNO was better than CNN and LSTM by preliminary study, seen from Figures S1–S6 in the Supporting Information. So we intended to develop an approach to combine mobile ECT with FNO to obtain instantaneous gas–solid distribution of nine cross-sectional slices at different heights aligned along the axial direction in the fluidized beds.

The working procedure of FNO is as follows: First, upgrade the input to a high-dimensional space through the network P based on Equation (15). Then, apply the Fourier layer and the activation function σ for multiple iterations through Equation (16). Finally, use the neural network Q to map to the target dimension via Equation (18). The detailed structure of the Fourier layer is expressed as Equation (17), which includes the following steps: the Fourier transform F, linear transformation R in the low Fourier modes, filtering in the high Fourier modes, and the inverse Fourier transform F^{-1}.

$$v_t(x) := P(a(x)), \forall x \in D \tag{15}$$

$$v_{t+1}(x) := \sigma(W v_t(x) + (K(a;\emptyset)v_t)(x)), \forall x \in D \tag{16}$$

$$\begin{cases} (K(a;\emptyset)v_t)(x) := \int \kappa(x,y,a(x),a(y);\phi)v_t(y)dy, \forall x \in D \\ (K(\phi)v_t)(x) := F^{-1}\left(R_\phi \cdot F(v_t)\right)(x) \end{cases} \tag{17}$$

$$y(x) := Q(v_{t+1}(x)), \forall x \in D \tag{18}$$

In this work, we adopted the Adam optimizer and set the hidden Layer parameter t as 4. The input of FNO is current gas–solid distribution $a(x)$ and the output $y(x)$ is a future gas–solid distribution that is updated with four iterations, which is shown in Figure 2.

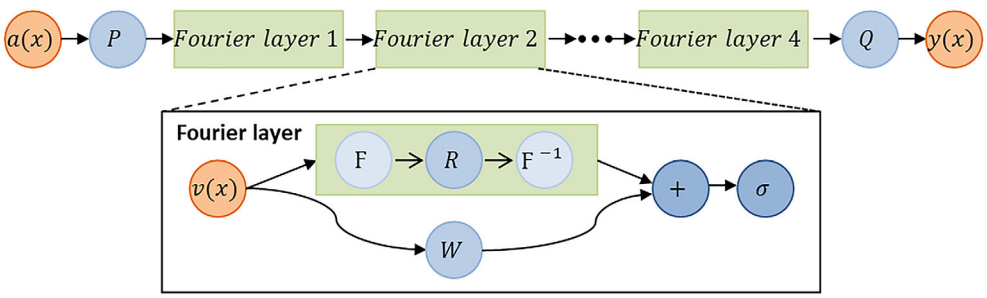

FIGURE 2 Flow chart of Fourier neural operator algorithm.

2.3 | 3D gas–solid distribution measurement strategy

Figure 3 shows the 3D gas–solid distribution measurement strategy by combing 2D mobile ECT with FNO method. In this strategy, we assumed that the 3D gas–solid distribution was in principle composed of N slices evenly distributed along the axial direction. These slices, following the order from the bottom to the top of the reactor, were numbered as 1, 2, 3, ..., n, ..., N. Thus the axial location of the n^{th} slices was $Z_n = (n-0.5)\Delta z$ with $\Delta z = H/N$ the distance between two adjacent slices and H the height of the measurement volume. As shown in Figure 3, the idea of this strategy is that, at any given instant t, while the mobile ECT provides the measurement of the cross-sectional gas–solid distribution of a specified slice n, the cross-sectional gas–solid distributions of the rest slices are predicted using the data-driven FNO method.

To realize our proposed strategy, it is essential to obtain a well-trained FNO model for predicting gas–solid distributions, as shown in Figure 4. In doing so, we first use the mobile ECT sensor to measure capacitance between electrodes for all slices and for each slice the sensor will stay for certain duration. Then measured capacitance will be used to reconstruct permittivity distribution using the Landweber iterative algorithm described by Equations (9)–(12), which will be further used to obtain the concentration distribution based on the parallel model described by Equations (13) and (14). Thus a large number of consequent frames of images of gas–solid distribution with time interval of Δt will be obtained for each slice. In fact, based on our results we found that, at any slices, the FNO, after pre-trained with these measured data, could be used to predict gas–solid distribution in the next six time intervals based on the data over the past 24 time intervals (The numbers of steps required for the prediction are not fixed. In fact, we have tried different setting for these numbers, and

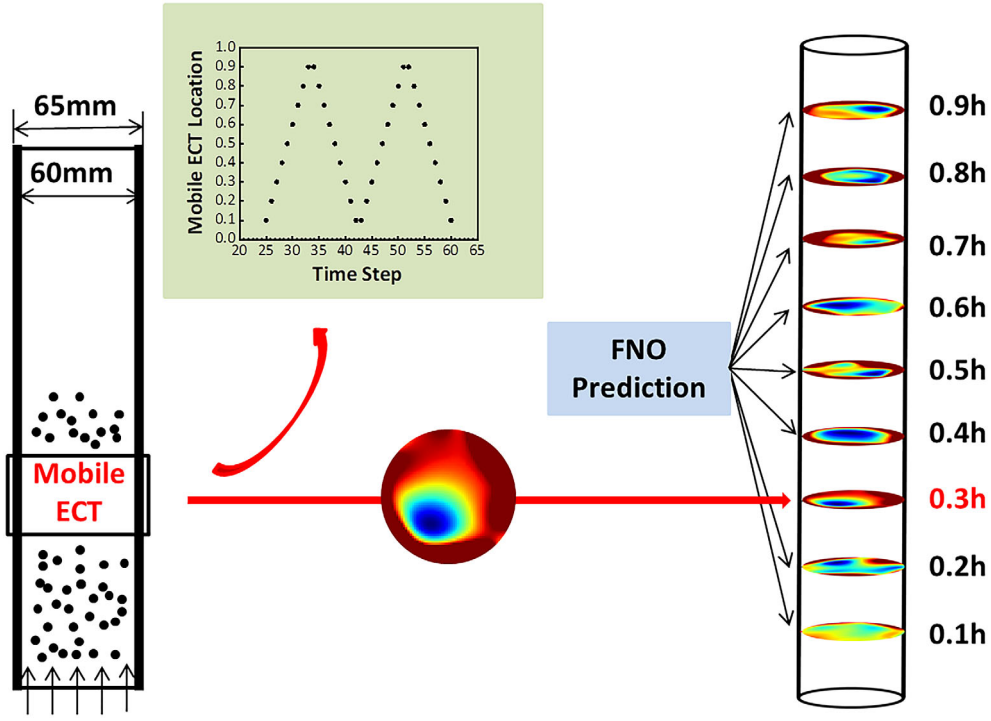

FIGURE 3 3D gas–solid distribution measurement strategy combing mobile ECT with FNO.

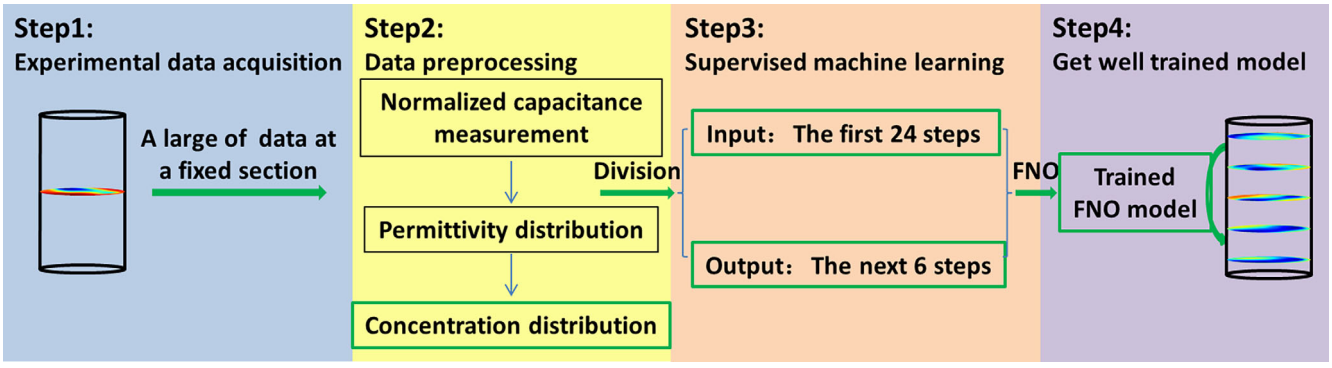

FIGURE 4 Flowchart for the training FNO model with mobile ECT measurement data.

found that more prediction steps result in lower accuracy. To balance prediction accuracy and time step horizon, we chose to use data from 24 steps to predict the data for the next 6 steps in the rest of this work) as illustrated in Figure S1. Here, the time intervals are typically 0.005 s. For these time intervals, FNO shows good prediction ability for fluidization process studied in our specific cases. We argued that the fluidization states between shorter intervals might be closely correlated. However, we believe that a careful examination is highly desired concerning the correlations between the ECT images with longer time intervals. Meantime, it has been also proven that FNO trained based on the measured data at only one slice could be well used to predict the gas–solid distribution at all other slices as seen from Figures S7–S13. This indicated FNO has the generalization ability for predicting the fluidization pattern at different spatial locations. In this sense, the well-trained FNO model is able to learn the correlation between data from different time and at different locations, even though fluidization is a dynamic process.

Figure 5 illustrates the prediction procedure of the pre-trained FNO for gas–solid distribution at different slices along the axial direction of the deep fluidized bed. It should be noted that the input of FNO model is the concentration distribution of the first 24 steps, so data volume m at each slice needs to exceed 24. At any instant t, we first calculated the axial location of mobile ECT based on its moving speed and then determined which slice the sensor was located. For this specified slice, we could obtain the measured image of gas–solid distribution. For all other slices, the image of gas–solid distribution would be predicted by the well-trained FNO model. In the prediction

TABLE 1 Physical properties of gas and solid particles in numerical simulations.

Gas	Density, ρ_g, kg/m^3	1.225
	Viscosity, μ_g, Pa·s	1.7894×10^{-5}
Particles	Density, ρ_s, kg/m^3	2500
	Viscosity, μ_s, Pa·s	10
	Diameter, d_p, μm	300

TABLE 2 Some model parameters used in the numerical simulations.

Property	Parameter
Viscous model	k-epsilon (2 eqn.)
Granular viscosity (kg/m^3)	Syamlal–O'Brien
Drag coefficient	Schiller–Naumann
Gravitational acceleration (m/s^2)	−9.81
Pressure–velocity coupling	Phase coupled SIMPLE
Discretization	First order upwind
Time step(s)	0.001

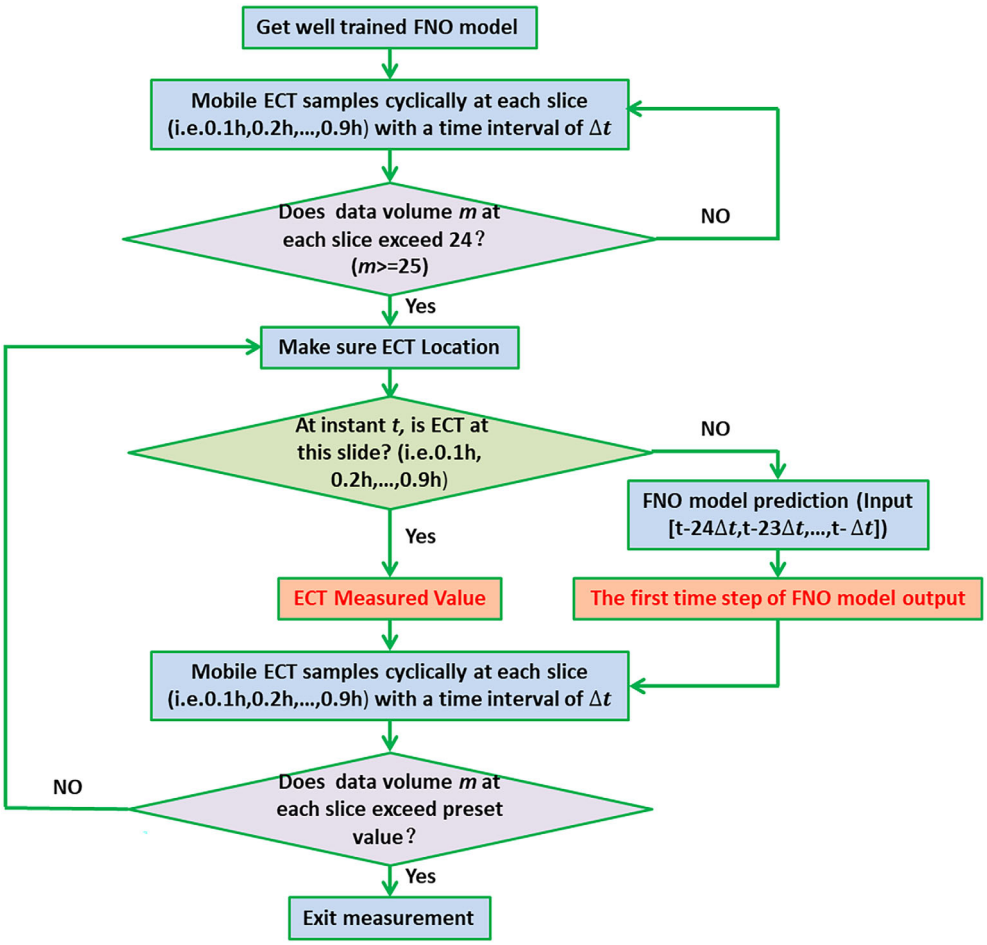

FIGURE 5 Procedure for predicting of gas–solid distribution at different slices along axial direction of a deep fluidized bed based on the pre-trained FNO.

FIGURE 6 Data division method.

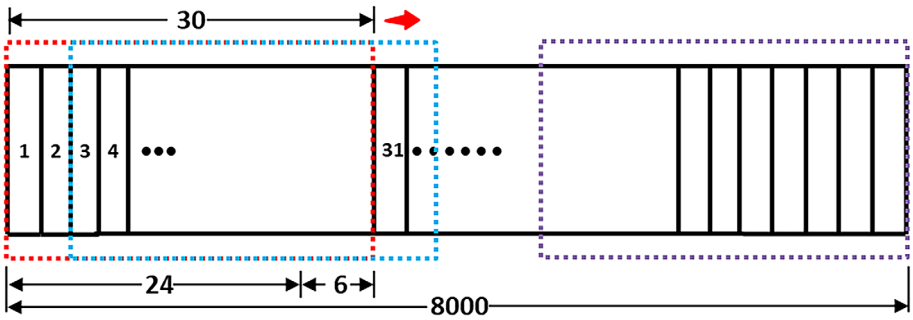

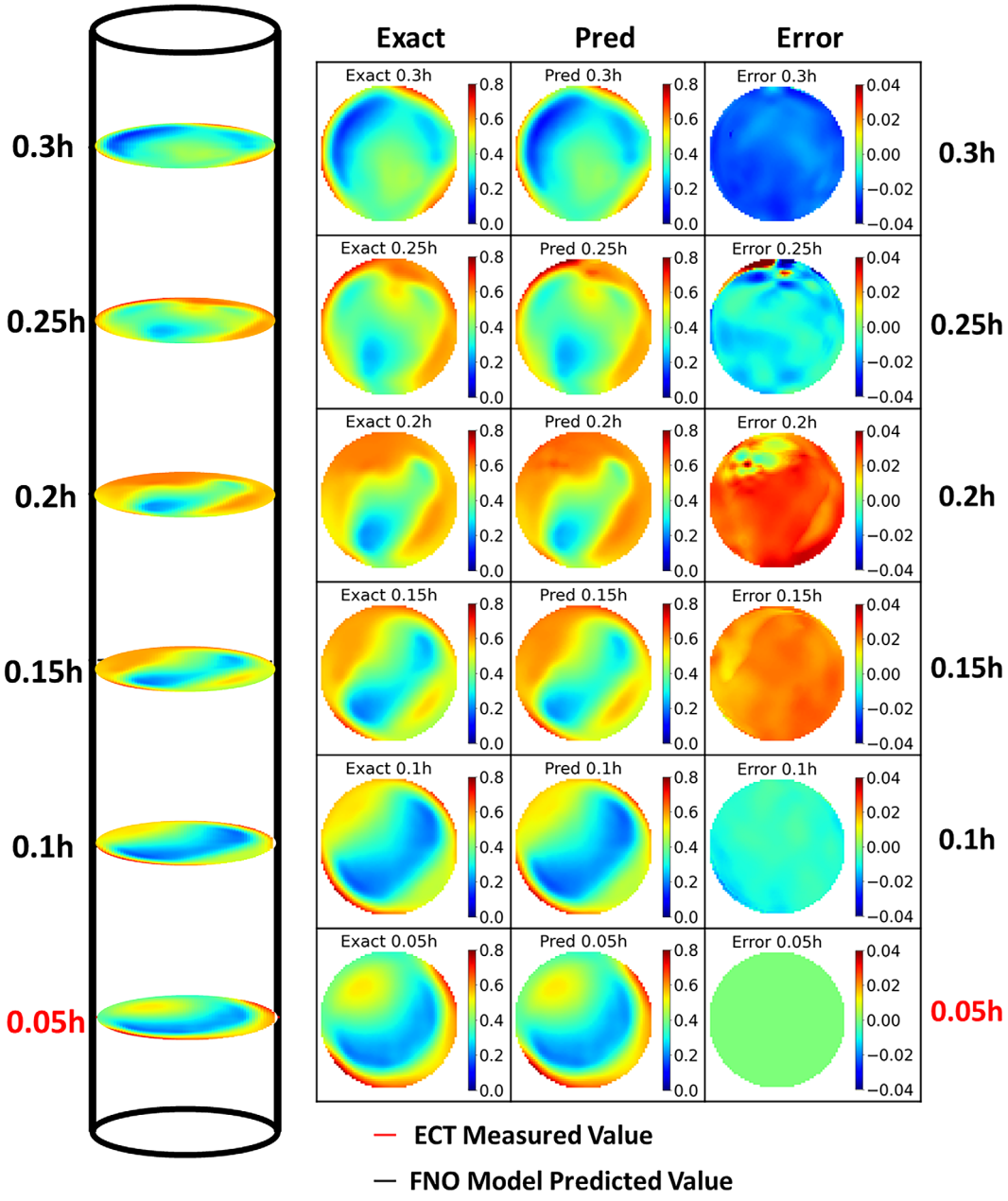

FIGURE 7 Ground truth and prediction of solid concentration, along with deviation at different slices in the bubbling fluidized bed at a specific instant.

of images of slice n, for example, the input was the images of gas–solid distribution of slice n at the instants including $t-24\Delta t$, $t-23\Delta t$, ..., $t-\Delta t$ and result was the first time step of FNO model output. Finally, all different slices of deep fluidized beds could get gas–solid distribution.

2.4 | Key hydrodynamic parameters

To further understand hydrodynamics of gas–solid two-phase flow inside fluidized beds, here we focused on two key parameters, that is, the Average solid concentration (ASC) and the equivalent bubble diameter (EBD). In this work, ASC was obtained via Equation (19):

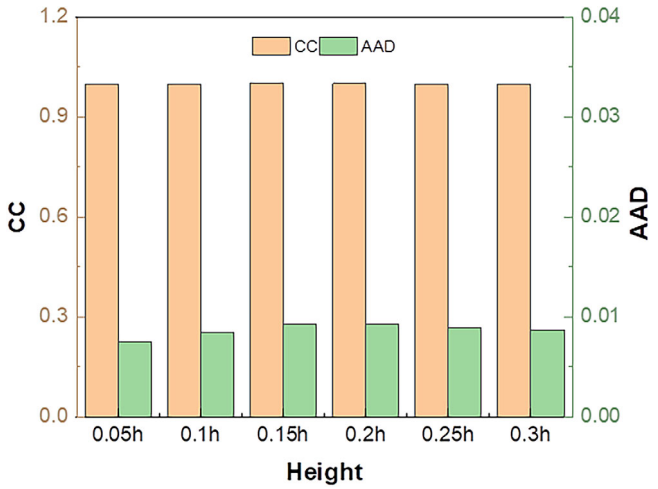

FIGURE 8 CC and AAD of gas–solid concentration distribution at different slices in the bubbling fluidized bed.

$$\overline{\widehat{\phi}} = \frac{\sum_{i=1}^{N} \widehat{\phi}_i A_i}{\sum_{i=1}^{N} A_i} \tag{19}$$

where $\widehat{\phi}_i$ was solid phase concentration of a single pixel, and A_i was the area of a single pixel.

EBD was obtained via Equation (20)[56]:

$$\overline{d} = \sqrt{4S/\pi} \tag{20}$$

The details for deriving EBD were as following. First, we needed to determine a threshold for solid concentration and then separated the bubbles and surrounding emulsion phases according to this threshold. Then, we counted the number of pixels for each bubble to obtain the bubble area S. So the equivalent bubble diameter could be estimated via Equation (20). In this work, a normalized threshold (ratio of actual solids concentration threshold to fixed bed solids concentration) of 0.9 was chosen to identify the boundaries of these quasi-bubbles.[52]

3 | RESULTS AND DISCUSSION

3.1 | Measurement evaluation criteria

The measurement results were needed to evaluate and thus several evaluation criteria were defined. First, we defined the solid concentration error *Err*, as shown in Equation (21).[51]

$$Err = \widehat{\phi}_i - \phi_i \tag{21}$$

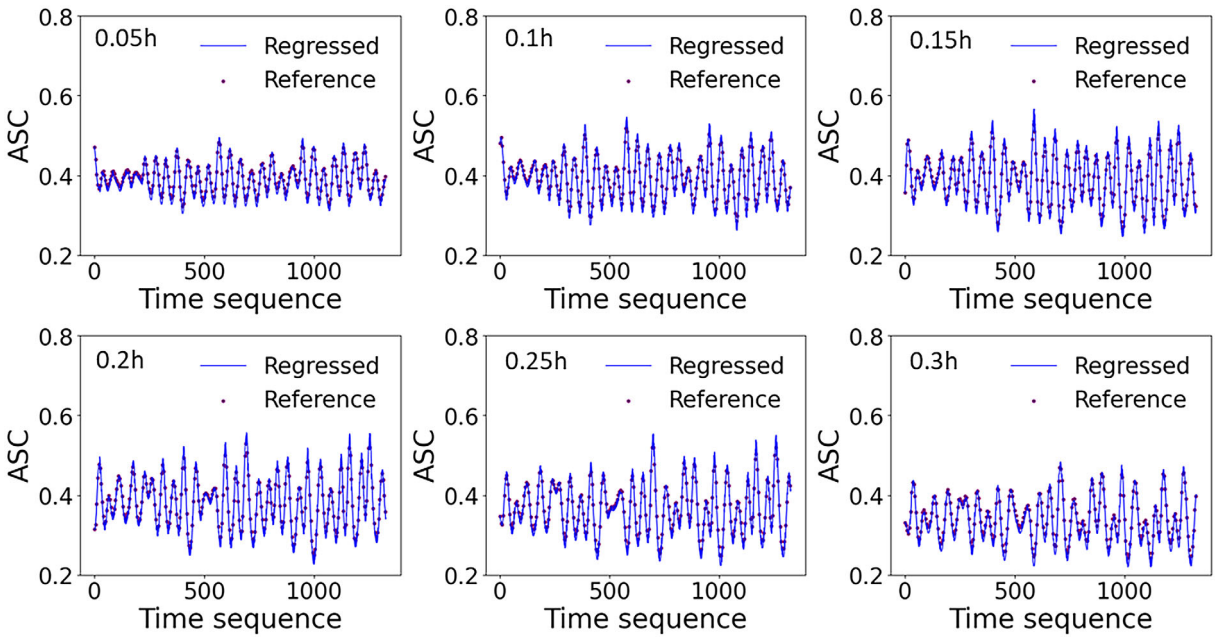

FIGURE 9 Referenced ASC and regressed ASC of gas–solid distributions at different slices in the bubbling fluidized bed.

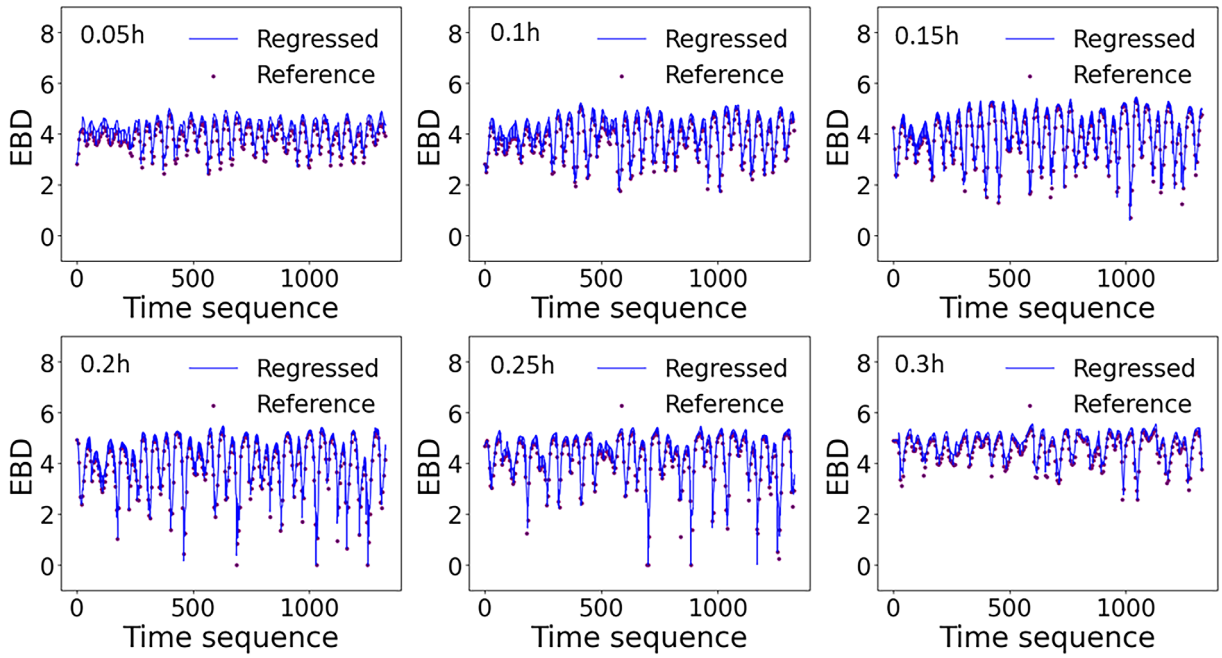

FIGURE 10 Referenced EBD and the regressed EBD of gas–solid distribution at different slices in the bubbling fluidized bed.

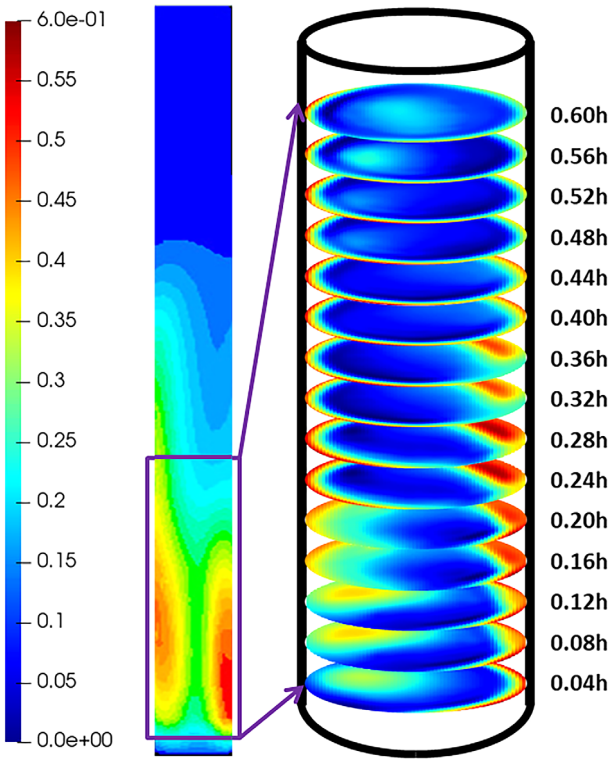

FIGURE 11 Ground truth and prediction of solid concentration at different slices in the turbulent fluidized bed at a specific instant.

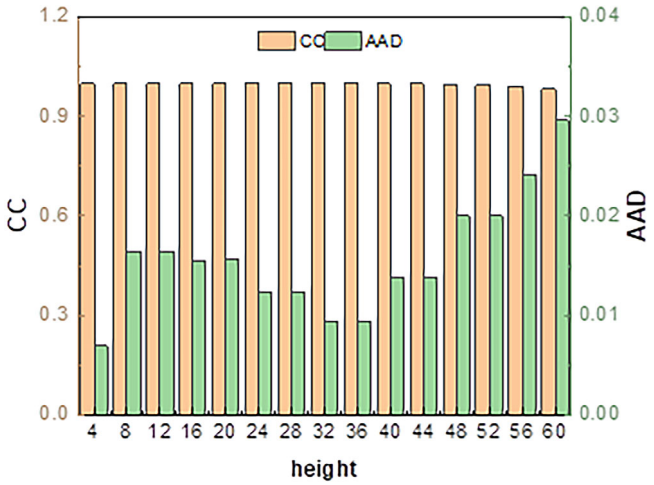

FIGURE 12 CC and AAD of gas–solid concentration distribution at different slices in turbulent fluidized bed.

To evaluate the quality of ECT images, we defined image correlation coefficient (CC),[29,57,58] and solid concentration average absolute deviation (AAD).[30] In fact, both AAD or RMS can be used as an evaluation indicator in reconstructing gas–solid concentration distributions. Note that RMS is the square root of the mean of squares of the differences between the predicted and true values, and AAD gives equal weight to all errors and RMS is more sensitive to large errors as the square term can amplify the large errors. We did some tests by use of either AAD or RMS as an evaluation indicator, and found that the corresponding gas–solid concentration distributions reconstructed only have minor difference. Therefore, we selected AAD as evaluation indicator in the rest of this work. The calculation methods for CC and AAD were given in Equations (22) and (23), respectively.

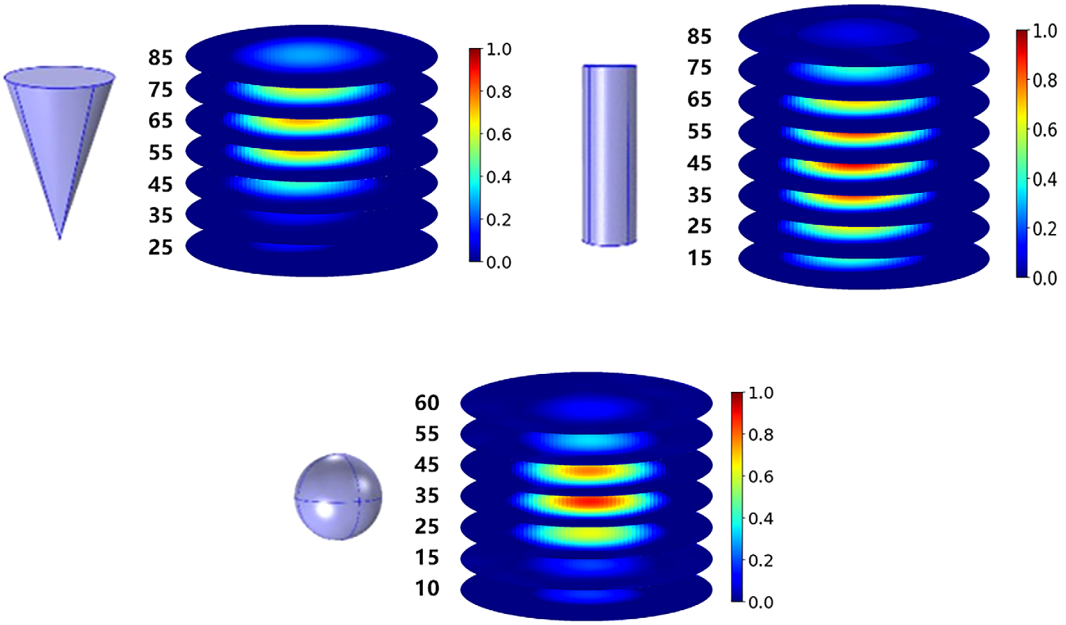

FIGURE 13 Exacted and reconstructed cone, cylinder, and sphere.

$$CC = \frac{\sum_{i=1}^{N}\left(\widehat{G}_i - \overline{\widehat{G}}\right)\left(G_i - \overline{G}\right)}{\sqrt{\sum_{i=1}^{N}\left(\widehat{G}_i - \overline{\widehat{G}}\right)^2 \sum_{i=1}^{N}\left(G_i - \overline{G}\right)^2}} \tag{22}$$

$$AAD = \frac{1}{N}\sum\nolimits_{i=1}^{N}\left|\widehat{\phi}_i - \phi_i\right| \tag{23}$$

Here $\overline{G}$ is the average actual permittivity that is obtained by averaging the measured permittivity G_i over all pixels, and similarly $\overline{\widehat{G}}$ is the average reconstructed permittivity that is obtained by averaging the reconstructed $\widehat{G}_i$ over all pixels. $\widehat{\phi}_i$ is the reconstructed solid concentration of single pixel, and ϕ_i is the actual solid concentration of single pixel.

3.2 | Numerical simulation verification

We first conducted 3D numerical simulations of a laboratory-scale fluidized bed, and used the simulation results to verify the proposed strategy. The fluidized bed with an inner diameter of 14 cm and a height of 1.5 m was simulated based on the Euler–Euler two-fluid model with Fluent 6.3. In the simulations, it is assumed that the air entered the fluidized bed with superficial gas velocity of 1.5 and 2.0 m/s, corresponding to bubbling and turbulent fluidization states respectively, and leaved the fluidized bed with the constant pressure condition. A grid with mesh size of $\Delta x = \Delta y = 8$ mm and $\Delta z = 7.5$ cm were implemented in the simulation. Thus there were a total of 3840 hexahedrons, with 192 CFD cells for each slice. For simplicity, the gas phase used in the simulation was air and the solid phase were Geldart B particles with a particle diameter of 300 μm. In the initial state, particles with 0.5 m height and 0.55 volume fraction were packed at the bottom of fluid bed. Physical properties of the two phases were listed in Table 1, and the model parameters applied were listed in Table 2.[59] In order to fully derive the bubbling characteristics in fluidized bed, the physical time for CFD simulations were set as 80 s, with 100 frames of images per second and a total of 8000 frames of data obtained.

In the bubbling state with superficial gas velocity of 1.5 m/s, we considered gas–solid distribution in the six cross-sectional slices at the height of 5, 10, 15, 20, 25, and 30 cm, represented by 0.05, 0.10, 0.15, 0.20, 0.25, and 0.30 h for 3D gas–solid distribution reconstruction. At each slice, a total of 8000 frames of images were obtained and processed to generate 7971 sample sets, as shown in Figure 6. These images, following the sequence of time, were numbered as 1, 2, 3, ..., i, ..., 8000. And the composition of the j^{th} sample was $[j, j+1, \ldots, j+29]$ where the first 24 steps (corresponding to $[j, j+1, \ldots, j+23]$) were the input of FNO model and the subsequent 6 steps (corresponding to $[j+24, j+25, \ldots, j+29]$) were the output of model.

We further divided the images at any given slice as training and test set by the ratio of sample numbers of 5:1. So for each given slice, there were 6642 samples (corresponding sample number j ranging from 1 to 6642) in the train set and 1329 samples (corresponding j ranging from 6643 to 7971) in the test set. At any instant t we considered the image for only one given slice as "measured image" and images for rest slices as "predicted images." To obtain "the predicted images," we need to first get a well-trained FNO. As discussed above, the FNO can be trained based on the 6642 samples at any given slice.

Figure 7 illustrates an example in which, at the specific instant, the "measured image" is at 0.05 h, and all other images are "predicted images" derived from FNO. Note that here the FNO was trained with 6642 samples obtained at 0.3 h. As can be seen, FNO trained by the

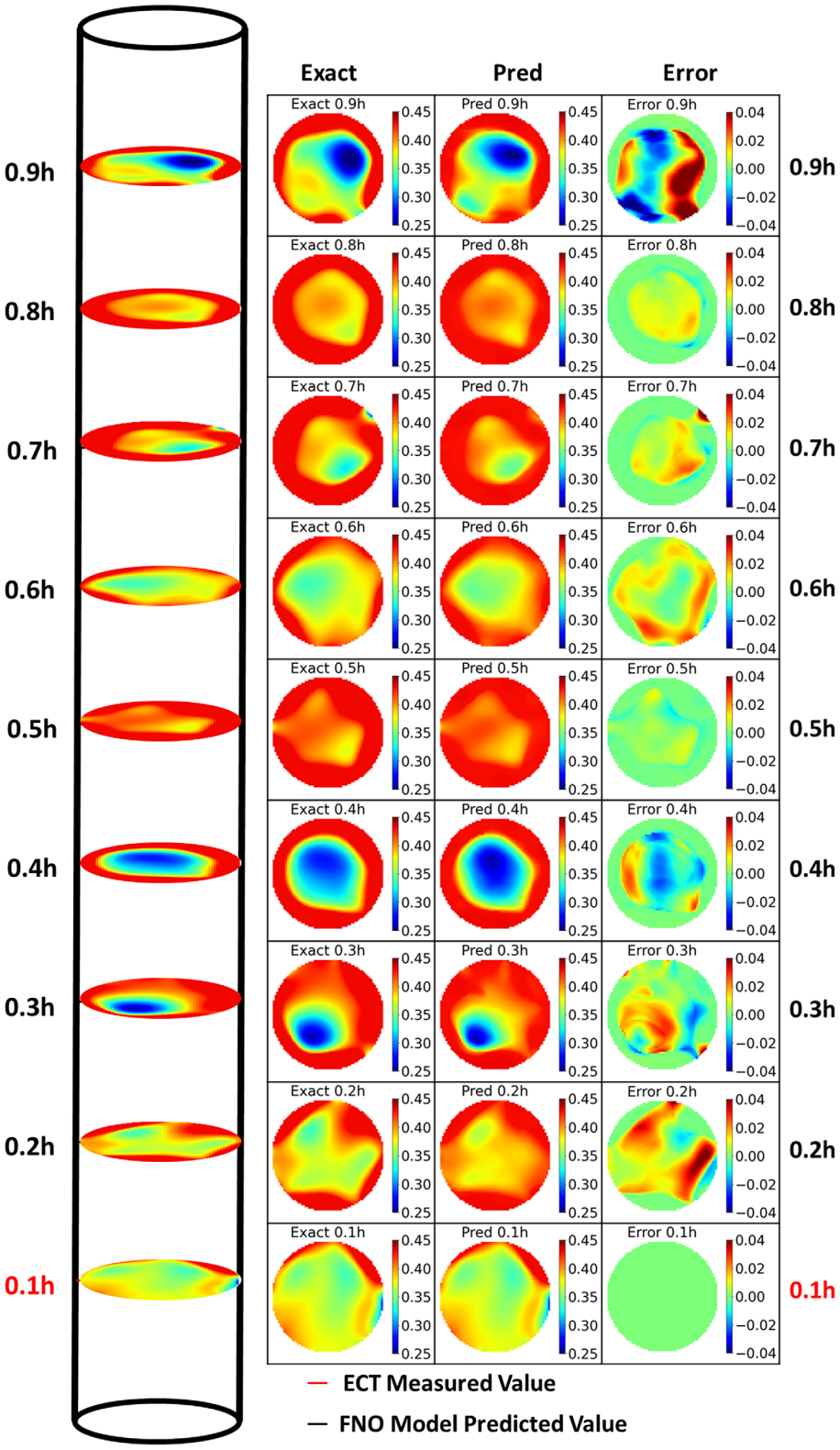

FIGURE 14 Observation and prediction of solid concentration, along with deviation at different slices in the actual experimental fluidized bed at a specific instant.

images at 0.3 h can be well used to predict images for all slices. The maximum absolute error of solid volume fraction is close to 0.04 at 0.3 h, while it is under 0.02 at other slices. Overall, at a given instant, the gas–solid distributions at all six slices can be recovered based on the proposed strategy.

We further verified the performance of the approach at continuous instants at all different slices in the test set of 1329 samples with sample number j ranging from 6643 to 7971. According to the proposed approach, where the ground truth of solid concentration corresponded to the images numbered from 6667 to 7995. We computed the CC and

AAD of gas–solid concentration distribution at 1329 continuous time steps based on ground truth and prediction. In Figure 8, the CC of the bubbling state at each slice is above 0.9 which is close to 1, the AAD of which is below 0.01 close to 0 at all continuous 1329 time sequences. All show the long-term good predicted performance.

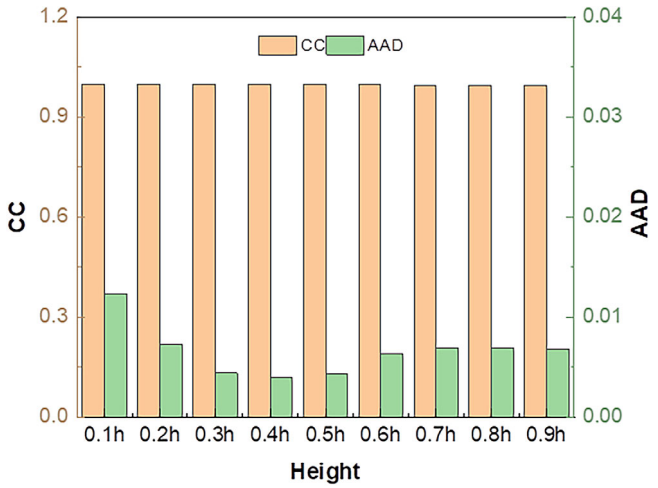

FIGURE 15 CC and AAD at different slices in the actual experimental fluidized bed.

Two key hydrodynamic parameters, that is, the average solid concentration and equivalent bubble diameter could be derived based on the gas–solid concentration distribution. Figures 9 and 10 show the relationships between the referenced ASC or EBD and the regressed ASC or EBD over time at each slice. It can be found that the regressed ASC or EBD matches the referenced ASC or EBD very well, indicating that our proposed strategy can well predict the key parameters of each slice for all continuous 1329 moments.

We also conducted simulations of turbulent fluidization with superficial gas velocity of 2.0 m/s. Here we considered the cross-sectional slices at the height of 4, 8, 12, 16, 20, 24, 28, 32, 36, 40, 44, 48, 52, and 60 cm, represented by 0.04, 0.08, 0.12, 0.16, 0.20, 0.24, 0.28, 0.32, 0.44, 0.48, 0.52, and 0.60 h for 3D gas–solid distribution reconstruction. Compared to that in the simulation of bubbling fluidization, more cross-sectional slices were considered in the simulation of turbulent fluidization because of a higher expansion of the fluidized bed. The numerical simulation parameters and data division method were the same as bubbling state. Here, in total 6642 train samples at 0.32 h were selected to train the model. Figure 11 depicts an example in which, at the specified instant, the "measured image" is

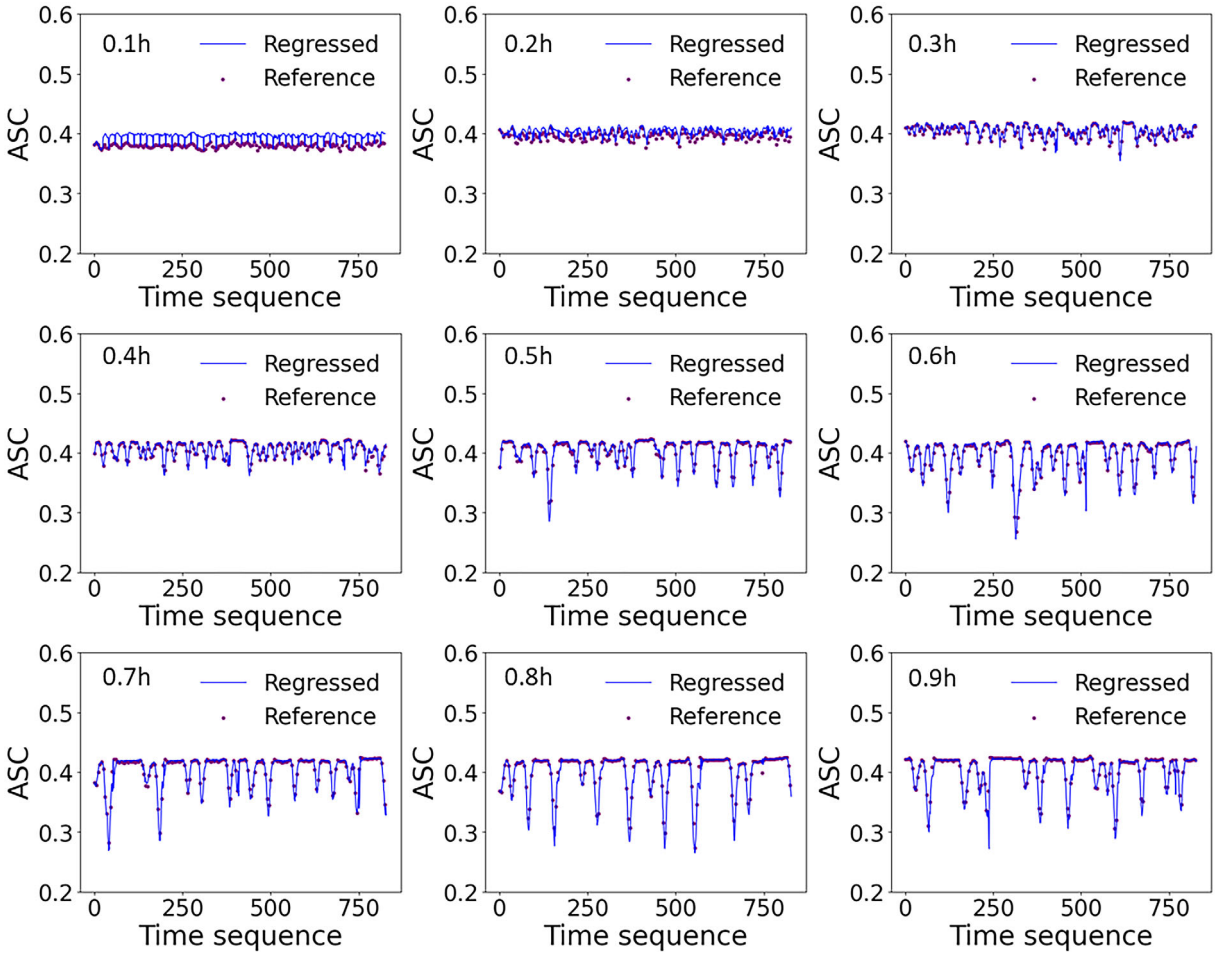

FIGURE 16 Referenced ASC and the regressed ASC of gas–solid distribution at different slices of the fluidized bed by ECT measurements.

at 0.04 h, and all other sections are "predicted images" derived from FNO model trained at 0.32 h. We can find the gas–solid distributions at all 15 slices can be recovered. From Figure 12, in test set of 1329 continuous time sequences, for each slice the CC of gas–solid concentration distribution is higher than 0.9, and AAD of which is all below 0.03 a little larger than bubbling fluidization. In the verification, similar CC and quite different AAD were obtained for the bubbling and turbulent fluidized beds. This can be attributed to the fact that the gas–solid concentration distribution of the turbulent fluidization changes more dramatically than that of the bubbling fluidization on the one hand, and, compared to CC, AAD is more sensitive and can amplify subtle differences. When the height exceeds 0.32 h, it appears as a whole that AAD increases with height. Overall, the proposed approach can also be applied to turbulent fluidized bed.

3.3 | Mobile ECT experiments

As shown above, our 3D CFD simulation of both bubbling and turbulent fluidization demonstrates that the 3D instantaneous gas–solid distribution could be obtained by combing mobile ECT measurement with FNO based machine learning method. In the following, we would further validate our approach by conducting experimental measurements.

We first verified the feasibility of the proposed approach by measuring some static objects using the single plane eight-electrode ECT sensor. In our current work, three static objects including a cone with height of 6 cm and diameter of 3 cm, a cylinder with height of 5 cm and diameter of 2 cm, and a sphere with diameter of 3 cm were considered. In Figure 13, we found that the height of cone was 6 cm based on ECT measurement results, which was consistent with height of the actual cone mold. We also measured the height of cylinder and sphere, and found that the reconstructed heights were 7 and 5 cm, respectively. The difference between the measured height and the actual one for these two molds, according to previous work,[24] could be attributed to the fact that ECT sensor has certain length, which would result in an axial averaging effect. Anyway, combing the mobile ECT with FNO method could provide a promising way for 3D reconstruction of static objects such as cone, cylinder and sphere.

We then studied the fluidization with mobile dual-plane 16-electrode ECT sensor. A series of 2D cross-sectional gas–solid

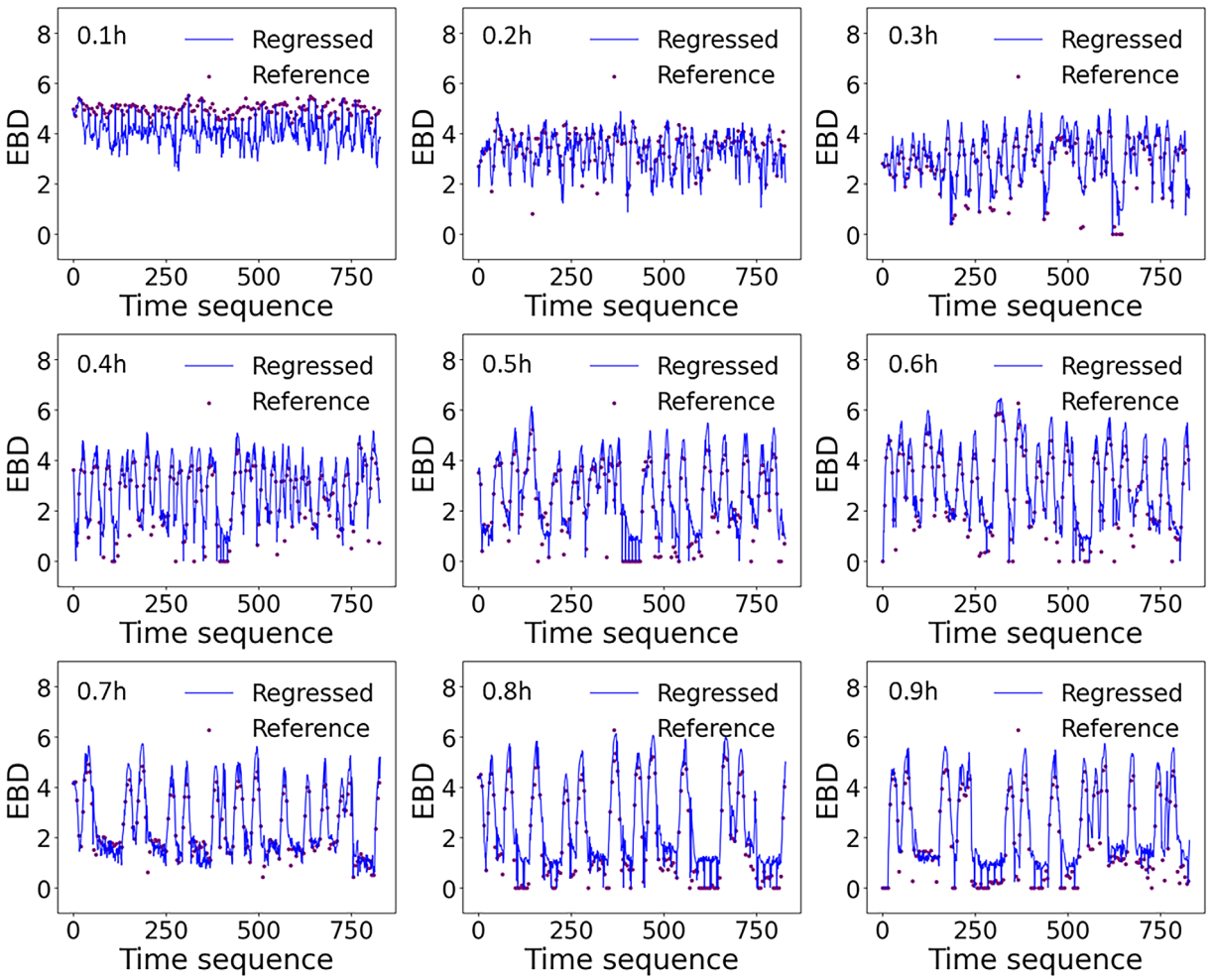

FIGURE 17 Referenced EBD and the regressed EBD of gas–solid distribution at different slices of fluidized bed by ECT measurements.

distributions at different slices had been measured using mobile ECT sensor, and 3D reconstruction results were obtained by use of FNO method. In ECT measurements, the Landweber iterative reconstruction algorithm and as well as the parallel concentration model were used for deriving the gas–solid distribution from the measured capacitance data. The data were divided into training set (4142 samples) and test set (829 samples). Here train set at 0.5 h was trained to get a well-trained model, which was then directly to be used for prediction at different slices for 829 continuous instants.

It should be noted that the measurements at different axial positions cannot be conducted simultaneously solely by the use of the mobile ECT. So we repeated the experimental condition five times to obtain approximately simultaneous gas–solid distributions at all different slices. Figure 14 depicts an example, in which, at the specified instant, the "measured image" is at slice of 0.1 h, and all other images are "predicted images" derived from FNO model trained at 0.5 h. The maximum absolute errors of solid volume fraction at all slices are under 0.02. We can find the gas–solid distributions at all nine slices can be recovered in the actual experimental fluidized bed.

We further verified the performance of the approach at continuous instants across all different slices in the actual experimental fluidized bed. Figure 15 shows the CC and AAD of gas–solid concentration distribution at each slice for 829 continuous moments in the actual experimental fluidized bed. All the CC values are above 0.9. Except for the AAD at 0.1 h, which is 0.012, the AAD for other slices is below 0.01.

From Figures 16 and 17, which are the relationship between referenced ASC or EBD of gas–solid concentration distribution and the regressed ASC or EBD over time at each slice for 829 continuous time sequences in the actual experimental fluidized bed, it can be found that at all slices referenced scatters match the regressed lines except 0.1 h.

Experiments with cone, cylinder and sphere proved that the measurement strategy, combining mobile ECT with FNO could be successfully applied to 3D reconstruction of static molds. Our experiments of fluidization further showed that the strategy could also be used to measure gas–solid distribution at different cross-sectional slices of the fluidized bed, which was evidenced by the regressed ASC and EBD of gas–solid distribution well matched the referenced ASC and EBD for the ground truth case.

4 | CONCLUSION

In this paper, we proposed to measure 3D instantaneous gas–solid distribution measurement by combining mobile ECT with Fourier neural operator based on the machine learning method. Especially two key hydrodynamic parameters, that is, the average solid concentration and equivalent bubble diameter, could be derived from the gas–solid distribution. This strategy was validated by both numerical simulations and experimental measurements of static molds.

For numerical simulations, both bubbling and turbulent fluidization were tested. In the bubbling state, six cross-sectional slices, along axial direction were selected for multi-plane prediction. In the turbulent fluidization state, due to the higher expansion of the fluidized bed, 12 cross-sectional slices at heights of 0.04, 0.08, 0.12, 0.16, 0.20, 0.24, 0.28, 0.32, 0.44, 0.48, 0.52 and 0.60 h were considered. In both cases, the image correlation coefficient CC values at all slices were also higher than 0.9 and the solid concentration average absolute deviation AAD was less than 0.03, showing that the proposed approach is promising.

The measurements of cone, cylinder, and sphere, in the meantime, illustrate that the current approach could be successfully applied to reconstruct 3D static objects in experiments with mobile ECT.

Finally, mobile ECT combined with the FNO method, was used to obtain 3D gas–solid distribution in fluidized bed. In the experiments, 4142 samples at the height of 0.5 h were used to train the FNO model, which was then applied to predict gas–solid concentration distribution simultaneously at nine different cross-sections along axial direction. It was shown that the CC of gas–solid distribution at all slices was higher than 0.9, and the AAD, except at 0.1 h was below 0.01. Both the regressed averaged solid concentration ASC and equivalent bubble diameter EBD matched the referenced values in ground truth cases very well. This demonstrated the feasibility of realizing 3D gas–solid distribution measurement in fluidized beds by combining 2D mobile ECT with FNO based on the machine learning method.

AUTHOR CONTRIBUTIONS

Cheng Zhang: Data curation (lead); formal analysis (lead); investigation (lead); methodology (equal); software (lead); validation (lead); visualization (lead); writing—original draft (lead). **Anqi Li**: Data curation (supporting); software (supporting); validation (supporting). **Chenggong Li**: Conceptualization (supporting); formal analysis (supporting); methodology (supporting); supervision (supporting). **Xue Li**: Funding acquisition (lead); supervision (equal); visualization (supporting); writing—original draft (supporting); writing—review and editing (lead). **Mao Ye**: Conceptualization (equal); data curation (supporting); formal analysis (supporting); funding acquisition (lead); methodology (supporting); project administration (equal); resources (supporting); supervision (lead); writing—review and editing (lead). **Zhongmin Liu**: Funding acquisition (lead); project administration (lead); resources (supporting); supervision (equal).

ACKNOWLEDGMENTS

This work was financially supported by the National Natural Science Foundation of China (Grant Numbers: 22108269, 22293021, and 22288101), and the DICP Innovation Foundation (Grant Number: I202238). We greatly appreciate senior engineer Shuanghe Meng in Dalian Institute of Chemical Physics, Chinese Academy of Sciences for the help with preparation of ECT sensors.

DATA AVAILABILITY STATEMENT

The numerical data from Figures 8, 12, and 15 are tabulated in the Supporting Information. The numerical simulation data in the bubbling fluidized bed and the corresponding FNO model predictions are available in Data S1. The results presented in Figures 7, 9, and 10 can be reproduced using these data with three scripts provided in Data S1.

Furthermore, numerical simulation data in the turbulent fluidized bed and the corresponding FNO model predictions are available in Data S2. The results presented in Figure 11 can be reproduced using these data with the script provided in Data S2. The ECT static experiment data and corresponding FNO model predictions are available in Data S3. These data support the results presented in Figure 13. The ECT fluidized experiment data and corresponding FNO model predictions are available in Data S4. The results presented in Figures 14, 16, and 17 can be reproduced using these data with three scripts provided in Data S4.

Data S1, S2, S3, and S4 can be downloaded from Google Drive at https://drive.google.com/drive/folders/1YIShwvf5DrWlxhC7S3wqI-MowHtAsmq4?usp=sharing.

ORCID

Mao Ye https://orcid.org/0000-0002-7078-2402

REFERENCES

1. Zhang CX, Qian WZ, Wei F. Instability of uniform fluidization. *Chem Eng Sci*. 2017;173:187-195.
2. Llop MF, Gascons N, Llauro FX. Recurrence plots to characterize gas-solid fluidization regimes. *Int J Multiphase Flow*. 2015;73:43-56.
3. Daw CS, Finney CEA, Vasudevan M, et al. Self-organization and chaos in a fluidized-bed. *Phys Rev Lett*. 1995;75:2308-2311.
4. Coppens MO, Van Ommen JR. Structuring chaotic fluidized beds. *Chem Eng J*. 2003;96:117-124.
5. Issangya AS, Karri SBR, Knowlton T, Cocco R. Use of pressure to mitigate gas bypassing in fluidized beds of fcc catalyst particles. *Powder Technol*. 2016;290:53-61.
6. Knowlton TM, Karri SBR, Issangya A. Scale-up of fluidized-bed hydrodynamics. *Powder Technol*. 2005;150:72-77.
7. Rudisuli M, Schildhauer TJ, Biollaz SMA, Van Ommen JR. Scale-up of bubbling fluidized bed reactors—a review. *Powder Technol*. 2012;217:21-38.
8. Garg SK, Pritchett JW. Dynamics of gas-fluidized beds. *J Appl Phys*. 1975;46:4493-4500.
9. Foscolo PU, Gibilaro LG. A fully predictive criterion for the transition between particulate and aggregate fluidization. *Chem Eng Sci*. 1984;39:1667-1675.
10. Van Der Hoef MA, Annaland MV, Deen NG, Kuipers JAM. Numerical simulation of dense gas-solid fluidized beds: a multiscale modeling strategy. *Annu Rev Fluid Mech*. 2008;40:47-70.
11. Xiong QG, Li B, Zhou GF, et al. Large-scale DNS of gas-solid flows on mole-8.5. *Chem Eng Sci*. 2012;71:422-430.
12. Zhu HP, Zhou ZY, Yang RY, Yu AB. Discrete particle simulation of particulate systems: a review of major applications and findings. *Chem Eng Sci*. 2008;63:5728-5770.
13. Johnsson F, Zijerveld RC, Schouten JC, Van Den Bleek CM, Leckner B. Characterization of fluidization regimes by time-series analysis of pressure fluctuations. *Int J Multiphase Flow*. 2000;26:663-715.
14. Van Ommen JR, Sasic S, Van Der Schaaf J, Gheorghiu S, Johnsson F, Coppens MO. Time-series analysis of pressure fluctuations in gas-solid fluidized beds—a review. *Int J Multiphase Flow*. 2011;37:403-428.
15. Almstedt AE, Zakkay V. An investigation of fluidized-bed scaling capacitance probe measurements in a pressurized fluidized-bed combustor and a cold model bed. *Chem Eng Sci*. 1990;45:1071-1078.
16. Li HZ, Zhu QS, Liu H, Zhou YF. The cluster-size distribution and motion behavior in a fast fluidized-bed. *Powder Technol*. 1995;84:241-246.
17. Shaffer F, Gopalan B, Breault RW, et al. High speed imaging of particle flow fields in cfb risers. *Powder Technol*. 2013;242:86-99.
18. Wang HF, Chen YP, Wang W. Scale-dependent nonequilibrium features in a bubbling fluidized bed. *AIChE J*. 2018;64:2364-2378.
19. Yang WQ, Liu S. Role of tomography in gas/solids flow measurement. *Flow Meas Instrum*. 2000;11:237-244.
20. Lewandowski B, Fertig M, Krekel G, Ulbricht M. Analysis of wake structures in bubbly flows using particle image velocimetry (PIV). *Chem Process Eng*. 2019;40:49-55.
21. Neogi A, Mohanta HK, Sande PC. Particle image velocimetry investigations on multiphase flow in fluidized beds: a review. *Flow Meas Instrum*. 2023;89:e102309.
22. Prasad AK. Particle image velocimetry. *Curr Sci*. 2000;79:51-60.
23. Zhang WB, Wang C, Yang WQ, Wang CH. Application of electrical capacitance tomography in particulate process measurement - a review. *Adv Powder Technol*. 2014;25:174-188.
24. Chandrasekera TC, Li Y, Moody D, Schnellmann MA, Dennis JS, Holland DJ. Measurement of bubble sizes in fluidised beds using electrical capacitance tomography. *Chem Eng Sci*. 2015;126:679-687.
25. Wang DW, Xu MY, Marashdeh Q, Straiton B, Tong A, Fan LS. Electrical capacitance volume tomography for characterization of gas-solid slugging fluidization with geldart group d particles under high temperatures. *Ind Eng Chem Res*. 2018;57:2687-2697.
26. Huang K, Meng SH, Guo Q, et al. High-temperature electrical capacitance tomography for gas-solid fluidised beds. *Meas Sci Technol*. 2018;29:104002.
27. Weber JM, Mei JS. Bubbling fluidized bed characterization using electrical capacitance volume tomography (ECVT). *Powder Technol*. 2013;242:40-50.
28. Xie CG, Huang SM, Hoyle BS, et al. Electrical capacitance tomography for flow imaging - system model for development of image-reconstruction algorithms and design of primary sensors. *IEE Proceedings G*. 1992;139:89-98.
29. Yang WQ, Peng LH. Image reconstruction algorithms for electrical capacitance tomography. *Meas Sci Technol*. 2003;14:R1-R13.
30. Banaei M, Annaland MV, Kuipers JM, Deen NG. On the accuracy of landweber and tikhonov reconstruction techniques in gas-solid fluidized bed applications. *AIChE J*. 2015;61:4102-4113.
31. Mckeen TR, Pugsley TS. The influence of permittivity models on phantom images obtained from electrical capacitance tomography. *Meas Sci Technol*. 2002;13:1822-1830.
32. Guo Q, Ye M, Yang W, Liu Z. A machine learning approach for electrical capacitance tomography measurement of gas-solid fluidized beds. *AIChE J*. 2019;65:e16583.
33. Mao MX, Ye JM, Wang HG, Zhang JL, Yang WQ. Evaluation of excitation strategy with multi-plane electrical capacitance tomography sensor. *Meas Sci Technol*. 2016;27:114008.
34. Agrawal V, Shinde YH, Shah MT, Utikar RP, Pareek VK, Joshi JB. Estimation of bubble properties in bubbling fluidized bed using ecvt measurements. *Ind Eng Chem Res*. 2018;57:8319-8333.
35. Liu S, Chen Q, Wang HG, Jiang F, Ismail I, Yang WQ. Electrical capacitance tomography for gas-solids flow measurement for circulating fluidized beds. *Flow Meas Instrum*. 2005;16:135-144.
36. Yang WQ. Design of electrical capacitance tomography sensors. *Meas Sci Technol*. 2010;21:042001.
37. Gu LL, Zhang YW, Zhu J. Wavelet denoising and nonlinear analysis of solids concentration signal in circulating fluidized bed riser. *Particuology*. 2020;49:105-116.
38. Huang K, Meng SH, Guo Q, et al. Effect of electrode length of an electrical capacitance tomography sensor on gas-solid fluidized bed measurements. *Ind Eng Chem Res*. 2019;58:21827-21841.
39. Banasiak R, Wajman R, Sankowski D, Soleimani M. Three-dimensional nonlinear inversion of electrical capacitance tomography data using a complete sensor model. *Prog Electromagn Res*. 2010;100:219-234.

40. Wang AN, Marashdeh Q, Motil BJ, Fan LS. Electrical capacitance volume tomography for imaging of pulsating flows in a trickle bed. *Chem Eng Sci*. 2014;119:77-87.
41. Weber JM, Bobek MM, Breault RW, Mei JS, Shadle LJ. Investigation of core-annular flow in an industrial scale circulating fluidized bed riser with electrical capacitance volume tomography (ECVT). *Powder Technol*. 2018;327:524-535.
42. Wang AN, Marashdeh Q, Fan LS. Ecvt imaging of 3d spiral bubble plume structures in gas-liquid bubble columns. *Can J Chem Eng*. 2014; 92:2078-2087.
43. Shen JJ, Meng SH, Wang J, Yang WQ, Ye M. Study on the shape of staggered electrodes for 3-d electrical capacitance tomography sensors. *IEEE Trans Instrum Meas*. 2021;70:1-10.
44. Li Y, Holland DJ. Optimizing the geometry of three-dimensional electrical capacitance tomography sensors. *IEEE Sens J*. 2015;15: 1567-1574.
45. Yang DY, Liu LJ, Feng WX. Experimental investigation of an internally circulating fluidized bed with 32-electrode electrical capacitance volume tomography. *Measurement*. 2018;127:227-237.
46. Li Y, Holland DJ. Fast and robust 3d electrical capacitance tomography. *Meas Sci Technol*. 2013;24:105406.
47. Ma LK, Kashanj S, Xu SL, Zhou JB, Nobes DS, Ye M. Flow reconstruction and prediction based on small particle image velocimetry experimental datasets with convolutional neural networks. *Ind Eng Chem Res*. 2022;61:8504-8519.
48. Fukami K, Fukagata K, Taira K. Super-resolution reconstruction of turbulent flows with machine learning. *J Fluid Mech*. 2019;870:106-120.
49. Eivazi H, Veisi H, Naderi MH, Esfahanian V. Deep neural networks for nonlinear model order reduction of unsteady flows. *Phys Fluids*. 2020; 32:e105104.
50. Nakamura T, Fukami K, Hasegawa K, Nabae Y, Fukagata K. Convolutional neural network and long short-term memory based reduced order surrogate for minimal turbulent channel flow. *Phys Fluids*. 2021; 33:e025116.
51. Li Z, Kovachki N, Azizzadenesheli K, et al. Fourier Neural Operator for Parametric Partial Differential Equations. 2020.
52. Li AQ, Meng SH, Huang K, Yang WQ, Ye M. On the concentration models in electrical capacitance tomography for gas-fluidized bed measurements. *Chem Eng J*. 2022;435:e134989.
53. Yang WQ, Spink DM, York TA, Mccann H. An image-reconstruction algorithm based on landweber's iteration method for electrical-capacitance tomography. *Meas Sci Technol*. 1999;10:1065-1069.
54. Du B, Warsito W, Fan LS. ECT studies of the choking phenomenon in a gas-solid circulating fluidized bed. *AIChE J*. 2004;50:1386-1406.
55. Yang WQ, Chondronasios A, Nattrass S, et al. Adaptive calibration of a capacitance tomography system for imaging water droplet distribution. *Flow Meas Instrum*. 2004;15:249-258.
56. Verma V, Padding JT, Deen NG, et al. Bubble dynamics in a 3-d gas-solid fluidized bed using ultrafast electron beam x-ray tomography and two-fluid model. *AIChE J*. 2014;60:1632-1644.
57. Ye JM, Wang HG, Li Y, Yang WQ. Coupling of fluid field and electrostatic field for electrical capacitance tomography. *IEEE Trans Instrum Meas*. 2015;64:3334-3353.
58. Ye JM, Wang HG, Yang WQ. Evaluation of electrical capacitance tomography sensor based on the coupling of fluid field and electrostatic field. *Meas Sci Technol*. 2016;27:074003.
59. Yuan ZL, Zhu LP, Geng F, Peng ZB. *Gas Solid Two Phase Flow and Numerical Simulation*. 1st ed. Southeast University Press; 2013.

SUPPORTING INFORMATION

Additional supporting information can be found online in the Supporting Information section at the end of this article.

How to cite this article: Zhang C, Li A, Li C, Li X, Ye M, Liu Z. Combing mobile electrical capacitance tomography with Fourier neural operator for 3D fluidized beds measurement. *AIChE J*. 2025;71(2):e18641. doi:10.1002/aic.18641